PCCP

PAPER

Cite this: *Phys. Chem. Chem. Phys.*, 2015, **17**, 2078

Confined platinum nanoparticle in carbon nanotube: structure and oxidation†

Guang-Feng Wei, Cheng Shang and Zhi-Pan Liu*

Received 15th September 2014,
Accepted 19th November 2014

DOI: 10.1039/c4cp04145c

www.rsc.org/pccp

A supported nanoparticle is dynamic in reaction conditions, but how this dynamic behavior is influenced by the support remains elusive. Using the stochastic surface walking global optimization method, herein, we report the structure, thermodynamics and catalytic properties of Pt nanoparticles inside and outside a carbon nanotube (CNT). We reveal that confined metal nanoparticles are, surprisingly, structurally more flexible at low temperatures but less likely to melt at high temperatures. By investigating the O_2 interaction with a Pt_{15} cluster inside and outside the CNT, we find that the low temperature structure versatility facilitates the *in situ* creation of favorable reaction sites, and thus maintains the catalytic activity of O_2 dissociation. The decrease of the population for the liquid-like structures (largely disordered) offers the higher stability of the confined nanocatalyst. The theoretical results are consistent with experimental findings for the enhanced antioxidation ability of the confined metal nanoparticles.

1. Introduction

Heterogeneous catalysts are often synthesized and operated under special environmental conditions such as high temperature and acidic solution.[1–3] Recent studies reveal that the structure of the nanosized catalyst is not invariant under reaction conditions,[4–10] and both the local surface sites and morphology may change dynamically. The structural complexity of the working nanocatalyst validates the traditional way to search for new catalysts, *i.e. via* exhaustive catalyst testing of a large combination of materials. For the rational design and optimization of better catalysts, the relationship between the catalyst structure and its activity needs to be established. Herein, we present a quantitative analysis on the structural versatility of nanocatalysts using recently developed stochastic surface walking (SSW) global optimization method.[11,12] Theory shows that the configuration space of a nanocatalyst is sensitive to the nanoparticle environment, and affects its activity and stability. This finding, together with the current knowledge on crystalline surfaces, may help to establish a quantitative correlation between the catalyst structure and its activity.

Shanghai Key Laboratory of Molecular Catalysis and Innovative Materials, Department of Chemistry, Key Laboratory of Computational Physical Science (Ministry of Education), Fudan University, Shanghai 200433, China. E-mail: zpliu@fudan.edu.cn

† Electronic supplementary information (ESI) available: The SSW algorithm; The comparison of DFT and force field for Pt_{15} cluster on CNT; XYZ coordinate of key structures, including Pt_{15}, $Pt_{15}O_2$, $Pt_{15}O_4$ and $Pt_{15}O_6$ particles inside and outside the CNT, Pt_{75} and Pt_{260} (only Pt atoms), CNT(10,10), CNT(14,14), the O_2 adsorption IS and dissociation TS on Pt_{15}, $Pt_{15}O_2$, $Pt_{15}O_4$ and $Pt_{15}O_6$ particles. See DOI: 10.1039/c4cp04145c

Metal–carbon composites have a wide application, such as sensing, electrode and catalytic materials.[13–15] Although the carbon material alone is generally a poor catalyst, carbon–metal composites often exhibit high catalytic activity and stability. The interplay between the metal nanoparticles and carbon substrate has thus attracted significant attention in recent years. Bao's group first showed that Fe nanoparticles inside a carbon nanotube (CNT) are much more resistant to oxidation than those loaded at the outer surface of a CNT,[16,17] and improved activity inside a CNT was also observed for other metal particles.[18,19] It was suspected that the metal–metal and metal–carbon interaction[20,21] inside and outside the CNT compete in a very different manner, which leads to the distinct catalytic activity. Dai and coworkers recently show that a Ni–Fe alloy nanoparticle hybrid with CNT can exhibit much higher electrocatalytic activity than nanoparticles or CNTs alone for water oxidation.[22] Similarly, the enhanced activity and stability of Pt nanoparticles encapsulated inside CNTs were also observed for the electrocatalytic methanol oxidation reaction[23] and asymmetric hydrogenation.[24] The structural variation of a small Pt cluster (Pt_{37}, Pt_{55}) on CNTs and graphene were also studied theoretically. Based on the canonical Monte Carlo calculations using the tight-binding potentials for Pt–Pt interaction and the Lennard-Jones potential for Pt–C interaction, Cheng *et al.*[25] predicted that the melting-like transformation temperature for Pt_{55} inside the (15, 15) and (20, 20) CNT are different (280 and 320 K, respectively), showing that the CNT has a significant effect on the structure and thermodynamics of the encapsulated Pt cluster. Wang and Johnson[26] by using first-principles molecular dynamics calculations found that, with and without the presence of the adsorbed H, the morphology of the Pt_{37}

cluster on graphene is very different. The adsorption of a high coverage of H helps to stabilize the truncated cuboctahedron shape of the cluster. These new findings indicate that the rich varieties of carbon microstructures could help to create unexpected reaction sites on metal particle that promote the activity and stability.

While theoretical tools are widely utilized nowadays for understanding the activity of metal surfaces, modern simulations, especially those involving quantum mechanics calculations, have so far not been able to capture the different structural and thermodynamics features of metal nanoparticles interacting with various carbon microstructures. The major obstacle is how to treat the high dimensional potential energy surface (PES) of the supported metal nanoparticles, where the canonical ensemble contains numerous minima and each is separated by high barriers of structural transformation. Recently, we developed the SSW method, a new global optimization method using second derivative information, to explore the PES of complex materials, and have demonstrated this in short-range Morse potential clusters,[12] large carbon fullerenes[12] and Boron clusters.[27] The new method opens up the possibilities to analyze the PES of supported transition metal nanoparticles for understanding the chemistry in reaction conditions.

The main focus of the current work is on the structure and PES of metal nanoparticles inside (M@CNT) and outside (M/CNT) CNTs. The metal nanoparticles concerned are Pt nanoparticles containing tens to hundreds of atoms, which are catalysts by themselves and also act as the nucleation sites in long-term catalyst operations. Specifically, we studied Pt_{15}, Pt_{75}, and Pt_{260} particles inside and outside CNTs. The CNT substrates utilized were (7, 7) (diameter (d) ~9.7 Å, length per unit cell (L) 2.2 nm, number of C atoms (N_c) 252), (10, 10) (d ~ 13.8 Å, L 4.5 nm, N_c 720) and (14, 14) (d ~ 19.3 Å, L 4.5 nm, N_c 1008) for supporting Pt_{15}, Pt_{75}, and Pt_{260}, respectively. Using the SSW method, we sampled the configuration space of Pt particles, and the key thermodynamic features for the particles inside and outside the CNTs were thus revealed. The catalytic O_2 dissociation on the Pt_{15} cluster inside and outside the CNT was also carried out to understand the various effects of the CNT on the structure, activity and stability of the metal particle.

2. Calculation details

The SSW method[11,12] interfaced with DFT and classical force field calculations was utilized for the global structure search. The SSW method is capable of surmounting the high barrier on PES and identifying the low energy minima, and also the efficiency of the method for structure searches has been demonstrated for clusters with complex PES (*e.g.*, short-range Morse potential clusters and large carbon fullerenes[21]). The algorithm of the SSW global optimization method is also included in the ESI.† The key parameters utilized in the SSW simulation are the same as those utilized previously for exploring the PES of carbon and Boron cluster,[12,27] *i.e.* Gaussian width of 0.6 Å and Gaussian potential of 10. The temperature utilized in the Metropolis Monte Carlo was set as 3000–5000 K. The higher temperature was used to verify the obtained GS structure. The structure of the CNT support was fixed during the PES sampling of the SSW structure search. The DFT energetics reported were finally converged with all the atoms, including the CNT, being allowed to relax.

For the supported Pt_{15} systems, the DFT calculations were performed using the SIESTA package[28,29] and the Troullier–Martins norm conserving the pseudopotentials.[30] The exchange–correlation functional utilized was at the generalized gradient approximation level, known as GGA-PBE.[31] The optimized double-ζ plus (DZP) polarization basis set with an extra diffuse function was employed for the metal. The orbital-confining cutoff was determined from an energy shift of 0.010 eV. The energy cutoff 150 Ry for the real space grid was used in the SSW structure search and a larger energy cutoff 250 Ry was used for converging the energetics of the O adsorption and dissociation of O_2 in the catalytic oxidation reactions.

While the spin-polarization was important for computing the energetics of the gas phase Pt_{15} cluster and the CNT with unsaturated edges,[32,33] the periodic CNT-supported Pt_{15}, both inside and outside, which concern us in this work, were found to be insensitive to the spin-polarization, due to the presence of Pt–C interactions and all the C atoms being sp^2 hybridized. For example, the spin polarization contribution to the total energies was calculated to be 0.01 eV for the Pt_{15}–CNT and 0.06 eV for Pt_{15}@CNT. For the O_2 interaction with CNT supported Pt_{15}, the adsorbed O_2 molecules on the Pt, as peroxo or superoxo, often remain to be spin-polarized, but the spin-polarization effect to the total energy is much reduced (considering that the O_2 molecule strongly prefers to be a triplet in the gas phase). Indeed, we found that the reaction barrier difference of the O_2 dissociation important for catalysis is less than 0.05 eV without and with the spin-polarization (we examined the O_2 dissociation reaction on Pt_{15}@CNT and Pt_{15}–CNT). In consideration of the Pt_{15}–CNT systems (more than 351 atoms) already being computationally demanding for the DFT calculations, and as here we are interested in the difference between the Pt_{15} inside and outside the CNT, we therefore only considered the spin-polarization for the gas phase Pt_{15} and omitted the effect for CNT supported Pt_{15} in the DFT calculations.

For the supported Pt_{75} and Pt_{260}, the Sutton–Chen[34] embedded potential was used to model the Pt–Pt interactions. The 12-6 Lennard-Jones potential fitted from the DFT data[35,36] (σ = 2.90 Å and ε = 0.0220 eV) was employed to describe the metal–carbon interactions. It is generally known that the force field calculations are much more reliable for very large systems, since the fitting parameters are generated by reference to the bulk properties such as the Sutton–Chen potential of Pt applied in this work. Therefore, we carefully validated our calculations by comparing the DFT and force field results in the Pt_{15} system, and these results can be found in the ESI.† Our results show that the Pt–Pt distance (the first neighbor distance) and the adsorption energy of Pt_{15}@CNT as calculated by DFT and by the force field calculations are rather close. We expect that the quality of the force field is enough to capture the essential physics of the system and to yield a qualitatively correct description for larger clusters,

for which the force field should be expected to yield even better results. Therefore, we studied Pt_{75} and Pt_{260} clusters inside the CNTs by using the force field. It might be mentioned that even the medium sized Pt_{75} system already contains 795 atoms (720 C atoms and 75 Pt atoms) in a very large unit cell (40 Å × 40 Å × 44.89 Å), which is already too demanding for DFT calculations.

The quasi-Newton l-BFGS method is used for geometry relaxation, up to the point when the maximal forces on each relaxed atom are less than 0.01 eV $Å^{-1}$. To correct the zero-point energy for the reaction barrier, the vibrational frequency calculations were performed *via* the finite-difference approach. The transition states (TSs) of the catalytic reaction were searched using the Constrained-Broyden-based TS-searching method.[37,38]

To compute the free energy change ΔG of O_2 adsorption and dissociation on Pt_{15} inside and outside the CNTs, we first obtained the reaction energy of each step (strictly speaking, the Helmholtz free energy change (ΔF) at 0 K, 0 bar), which is directly available from the DFT total energy (ΔE) after the ZPE correction. For oxygen molecules in the gas phase, it is essential to take into account the large entropy term at 298 K. To describe the gas phase O_2 free energy, it is possible to either compute O_2 directly, or *via* the reaction formula $H_2O \rightarrow 0.5O_2 + H_2$, using the computed G of H_2O and H_2 and the experimental ΔG of the reaction. The later calculations involve non-spin-polarized calculations of H_2O and H_2 (but require experimental data). In the computation of O_2 dissociation on metals, it is generally found that the latter approach better describes the energetics compared to the experimental rate data.[39–41] This is because for O_2 adsorption on metal surfaces, the 2p orbital of the O_2 molecule interacts strongly with the Pt 5d orbitals and thus, the magnetic moment of O_2 is largely quenched. Thus, we utilized the standard thermodynamic data to obtain the temperature and pressure contributions, where the G of O_2 was derived as $G[O_2] = 4.92\ (eV) + 2G[H_2O] - 2G[H_2]$ by utilizing the oxygen evolution reaction equilibrium at the standard conditions.[42,43]

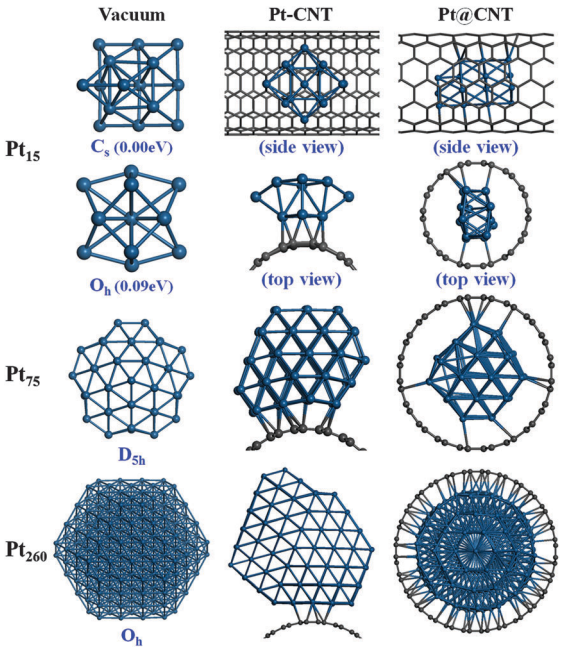

Fig. 1 The ground state structures for Pt_{15}, Pt_{75}, and Pt_{260} particles in vacuum and in the presence of CNTs from a SSW global structure search (outside CNT: Pt–CNT and inside CNT: Pt@CNT). DFT is utilized for describing the PES of Pt_{15} systems, whereas the classical potential is used for Pt_{75} and Pt_{260} systems.

3. Results and discussion

3.1 Global structure search of Pt nanoparticles interacting with CNTs

For Pt_{15}, we utilized first principles DFT calculations in combination with SSW to explore the PES. In the SSW structure search, we performed four parallel runs, and up to 500 minima were collected in the first stage, from which the most stable configuration was obtained. Next, we verified the result from the most stable configuration of the first stage and collected another 300 minima. This process was repeated until no more stable configurations were identified at this stage of verification. For the two large Pt nanoparticles (Pt_{75}, ~1.1 nm and Pt_{260}, ~1.5 nm), where running DFT calculations is prohibitive for a global structure search, we switched to the classical force field calculations[34–36] to describe the PES. The detail of the classical force field used here and the comparison with the DFT results of the Pt_{15} system can be found in the detailed calculations and also in the ESI.† For these systems, eight parallel runs were performed in the SSW structure search, and up to 16 000 minima were collected in the first stage. From the most stable configuration of the first stage, 10 000 minima were further searched to verify the result. In total, for Pt_{15}, Pt_{75}, and Pt_{260} 2058, 57 000 and 56 910 minima (including all the structures from both inside and outside the CNT) were obtained from the SSW trajectories, respectively. These minima from the SSW trajectories were then utilized to analyze the configuration space of the Pt nanoparticles inside and outside the CNT, and the results are detailed in the following.

Pt_{15} was regarded as a magic number size in vacuum.[44] As shown in Fig. 1, from our DFT calculations, the most stable form of free Pt_{15} has two likely structures with close energies (difference <0.1 eV). The ground state minimum (GS) is a capped square pyramid structure with a C_s symmetry that looks like a pyramid with an extra one atom near the apex; and the second lowest minimum (SLM) is a tetrakis hexahedron of O_h symmetry. For the large Pt particles, the GSs based on the Sutton–Chen potential were determined previously[45] and have been confirmed in this work using SSW. These two particles possess a high symmetry structure: Pt_{75} is a magic number with a D_{5h} icosahedron structure, and Pt_{260} is a truncated octahedral face-centered-cubic (fcc) packing structure with O_h symmetry, as expected from the Wulff construction rule.

The predicted GS inside and outside the CNT are also illustrated in Fig. 1. It can be seen clearly that the structure of the Pt_{15} cluster with the support are very different, no longer being either an O_h cubic or a C_s pyramid in vacuum. For Pt_{15}–CNT, a C_{2v} non-wetting 2-layer structure is the most stable, where six Pt atoms

are in close contact with the CNT surface and the other nine Pt atoms are in the second layer. By counting the Pt–Pt and Pt–C bonds, we found that four Pt atoms have nine coordinations, but the other Pt atoms have quite low coordination, the lowest coordination number of Pt being three (two terminal Pt atoms, see ESI,† Fig. S3). By contrast, Pt_{15}@CNT forms a short twisted rod, filling the inner space of CNT, with all the atoms effectively interacting with the inner surface of the CNT. The twisted rod has a non-fcc packing motif and contains four Pt layers, with the normal direction of the layers being along the CNT axis. The coordination of Pt inside the CNT is generally larger compared to the Pt outside the CNT. There are four and eight Pt atoms with eight and seven coordinations, respectively, and the lowest coordination number of Pt is four (one terminal Pt atom, see ESI,† Fig. S3). Consistently, the exothermicity of the adsorption of the Pt cluster (with respect to the gas phase Pt_{15} GS) is slightly larger inside the CNT compared to that outside the CNT, being −3.87 eV for Pt_{15}@CNT and −3.55 eV for Pt_{15}–CNT. It should be mentioned that, without the support, these two structures of Pt_{15}, outside and inside the CNT, are in fact very unstable in vacuum, being 3.3 and 4.2 eV less stable than the GS in vacuum.

We noted that Hu *et al.* investigated Pt_{13} and Pd_{13} on the dehydrated (100) surfaces of γ-Al_2O_3, both of them exhibiting biplanar structures.[46] This is quite similar to the GS structure of Pt_{15}–CNT. They further related the wetting of metal particles on the support to the particle-support interaction energy (the energy difference between the total energies of supported systems and the energies of the particle and support at the deformed geometry after the adsorption). Compared to the reported Pt_{13}–alumina interaction strength (−8.2 eV), our calculated value for the Pt–CNT interaction energy was quite close, −8.1 eV in Pt_{15}@CNT, but slightly smaller in absolute value, −6.9 eV in Pt_{15}–CNT. This may explain the formation of the similar biplanar structures in these systems.

The large structural difference of Pt nanoparticles with and without the CNT is observed similarly in the Pt_{75} and Pt_{260} systems (Fig. 1). In the presence of CNTs, the GS structures of Pt_{75} and Pt_{260} are no longer the high symmetry ones found in vacuum, *i.e.* D_{5h} for Pt_{75} and O_h for Pt_{260}, but adapt to the shape of the CNTs. For Pt_{75}–CNT and Pt_{260}–CNT, the GS structures belong largely to the fcc packing structure, with the defect layers at the interface with the CNTs. For Pt nanoparticles inside CNTs, while the GS structure of Pt_{75}@CNT is still largely a fcc packing structure, it is not particularly more stable than the other less stable structures, many of which have a completely different structure, *i.e.* a twisted rod structure similar to Pt_{15}. In the largest particle investigated, Pt_{260}@CNT, we found that the helix twisted rod structure is the GS, not the fcc packing structure. Apparently, this helix rod structure can maximally increase the number of Pt–C bonds by adapting the particle's shape to the curvature of the carbon wall. From the minima collected from SSW, we can interpret that unlike that of outside the CNT, the PES landscape of Pt nanoparticles inside the CNTs has two obvious funnels, a twisted rod structure and a fcc packing structure, which indicates that the presence of the CNT has a different influence on the PES of the Pt particles. Therefore, it would be interesting to analyze the configuration space of the Pt nanoparticles inside and outside the CNT and understand the thermodynamic properties.

3.2 The structure versatility of CNT-supported Pt clusters

Fundamental thermodynamics tells us that the GS structure can represent only the physical properties at the low temperature limit. To understand the thermodynamics of a catalyst at reaction conditions, other possible morphologies of metal nanoparticle must be taken into account (*e.g.* thinking that the CNT can distort the structure of Pt_{15} by 3–4 eV higher than the GS in vacuum). This would require knowledge on the partition function on PES, which is however expensive to compute due to the extremely large number of microstates (the number of minima is estimated to be 10^3 for Pt_{15} and 10^{29} for Pt_{75} (ref. 47)). Nevertheless, we can choose the representative minima on PES to construct the configuration component of the partition function, since we are only interested in the difference between the two similar systems (inside and outside the CNT), not the absolute thermodynamics quantity. By "representative minima," we mean that it is necessary to remove the duplicate structures (energetically degenerate) when investigating the thermodynamics, because the minima visited by the SSW simulations contain identical structures, such as the permutation isomer.

Herein, we calculated the density of states of the minima (DOS-m) by using all the distinct minima from the SSW trajectories. The minima with energy differences of more than 0.1 meV were considered to be distinct and were utilized in the plot. The DOS-m describes the transformed PES explored by the SSW method. The concept of a transformed PES was introduced by Wales[48] for understanding the thermodynamics of gas phase particles. One major difference between the transformed PES and the real PES is the lack of the vibrational component of quantity on the transformed PES (most global optimization methods, including the SSW method, quench all the structures to the minima). Because it is the low energy solid-like structures (where the vibrational component are similar between structures) that are concerned in catalysis, the configuration space sampled from the DOS-m should reveal the differences between the real PES for metals inside and outside the CNT. To understand the thermodynamics from DOS-m, the heat capacity (C_v) of the transformed PES can be calculated using eqn (1) and (2). In the equations, the internal energy of the transformed PES ($\tilde{U}$) is summed over all the distinct minima, and the calculated C_v corresponds to the configuration component of the heat capacity.[48]

$$\tilde{U} = \frac{\sum_i E_i e^{-(E_i - E_0)/k_B T}}{\sum_i e^{-(E_i - E_0)/k_B T}} \quad (1)$$

$$C_v = \left(\frac{\partial \tilde{U}}{\partial T}\right)_V \quad (2)$$

The DOS-m for Pt_{15} and Pt_{75} inside and outside the CNT are shown in Fig. 2, providing a 1-D overview for the PES of the supported Pt particles. By comparing the DOS-m for the Pt_{15}@CNT and Pt_{15}–CNT, we can identify some interesting characteristics that distinguish the two environments. The most obvious feature is the

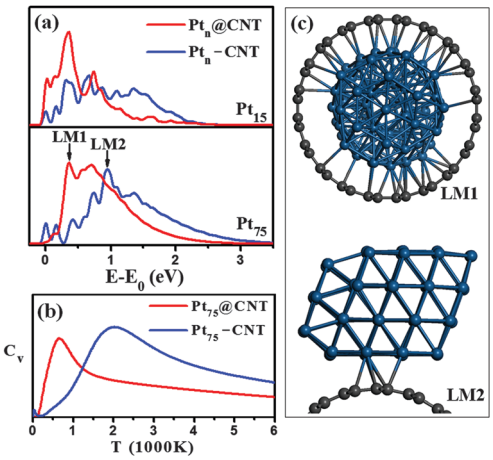

Fig. 2 (a) Density of states of the minima (DOS-m) for Pt_{15} and Pt_{75} particles inside and outside the CNT. All the minima are from the SSW trajectories at 5000 K. (b) Configuration component of the heat capacity for Pt_{75} systems. (c) Typical local minimum structure of Pt_{75} from the highest DOS-m peak in Fig. 2a.

narrowing of the energy gap between the GS and the SLM on going from the outside to the inside of the CNT. Consistently, the population of the low energy structures increases for the nanoparticle inside the CNT. Additionally, the largest peak in DOS-m shifts downwards in energy for Pt@CNT, compared to that for Pt–CNT. This is because the higher energy states (>1 eV above GS), mostly the liquid-like structures, are much reduced in density for the nanoparticle inside the CNT. The same features of PES are also observed for the larger Pt_{75} particle interacting with CNT (see Fig. 2), using the classical potential.

Based on eqn (1) and (2), we calculated the configuration component of the heat capacity C_v as shown in Fig. 2b for the Pt_{75} system, where a large database of minima is available. It was surprising to find that Pt_{75}@CNT exhibited its main C_v peak at a much lower temperature compared to Pt_{75}–CNT. This indicated that the Pt particle inside the CNT is structurally more flexible at low temperature regions and has larger configuration entropy.

By closely inspecting the structures, we can understand the heat capacity curve as follows. The PES landscape of the Pt nanoparticle inside the CNT is more complex and shows two obvious funnels. The surface atoms of the Pt nanoparticle inside the CNT can shift collectively at only low energy cost, due to the compensation of the external metal–carbon bonding, and thus there are many distinct low energy structures. For example, we show in Fig. 2c a typical structure at the peak of DOS-m for Pt_{75}@CNT, which is completely different from GS, but is only 0.3 eV higher than GS. Additionally, the particle inside the CNT is very difficult to expand in volume due to the Pauli repulsion of CNT (*i.e.* due to confinement), and thus the liquid-like structures at the high temperatures are largely diminished, as seen from the SSW trajectories. By contrast, for the Pt particle outside the CNT, the structural deformation requires overcoming a higher barrier and thus incurs a large energy cost because of the exposure of the low coordination sites. For comparison, we also show in Fig. 2c a typical structure at the peak of DOS-m for Pt_{75}–CNT, which is still a fcc structure but is 1 eV higher than GS. Due to the lack of confinement, the particle outside can expand and melt to the liquid-like structures at high temperatures. Interestingly, we noticed that a similar CNT confinement effect has been reported for water structures.[49,50] For a CNT diameter below 1.1 nm, water molecules tend to form a pentagon structure to fit with the curvature of the CNT, which is similar to what we observed for Pt particles inside the CNT (below 2 nm).

The modification of PES by the substrate affects the thermodynamics of the Pt particle and thus, should have a strong influence on the catalytic behavior. Since the local surface sites play an important role in heterogeneous catalysis,[51] we examined the local structure features of the Pt particles. We plotted in Fig. 3 the Pt–Pt distance distribution function inside and outside the CNT from the minima collected from the SSW trajectories. For comparison, each plot was normalized according to the area of the first Pt–Pt distance peak at $\sim$2.7 Å, which corresponds to the shortest Pt–Pt bond length. One immediate observation is that the Pt nanoparticles inside CNTs have much less probability to possess and expose the {100} facet, which is an important characteristic for the fcc-packing metal. For the Pt_{15} rod inside a CNT, the peak around $\sqrt{2}a$ (a = 2.7 Å) is diminished. Similarly, for the larger size Pt particles, the same attenuation of the $\sqrt{2}a$ peak occurs (Fig. 3). This structural feature is consistent with the structural versatility of Pt particles inside CNTs, where new non-fcc structures (the twisted rods) emerge at low temperatures, being the GS structure for Pt_{15}@CNT, Pt_{260}@CNT, and the SLM for Pt_{75}@CNT.

It might be mentioned that we also examined the Pt–C distance distribution for Pt_{15} inside and outside CNTs from the minima collected from the SSW trajectories (as shown in ESI† Fig. S4). Being different to the Pt–Pt distance distribution function in Fig. 3, the Pt–C distance distribution is in fact quite continuous (*i.e.* no sharp peaks at certain distances), starting from the shortest Pt–C distance at $\sim$2.2 Å. This is because the relatively high density of C atoms in the CNT near the Pt cluster

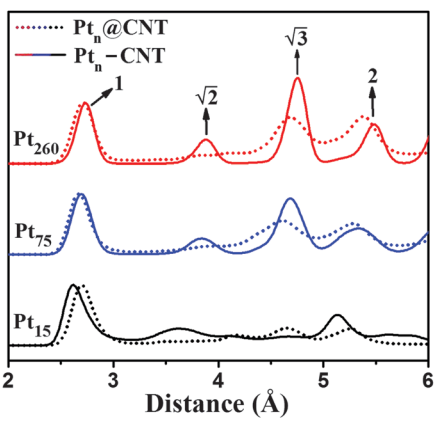

Fig. 3 Pt–Pt distance distribution for the Pt_{15}, Pt_{75}, and Pt_{260} inside and outside the CNT. All the minima are from the SSW trajectories at 5000 K.

and the interface Pt atoms can bond with up to 6 C atoms, with the distances ranging from 2.2 to 3.0 Å. Since the Pt cluster inside the CNT has more chance to interact with the C atoms, as expected, it has more Pt–C bonds (within 2.8 Å, Table S2, ESI†), which is consistent with the larger exothermicity of the adsorption of the Pt cluster inside the CNT.

3.3 Electronic structure and structural versatility for higher activity and stability

Having shown that the geometrical structure and the thermodynamic properties are quite different for Pt nanoparticles inside and outside the CNT, we are now at the position to examine the catalytic behavior of these Pt particles. It is known that the electronic structures of surface metal atoms, *e.g.*, the localized d states, can influence strongly the catalytic properties of nanoparticles. However, to check this, we first plotted the density of states projected onto the 5d orbitals (pDOS) of all the Pt atoms for the GS structures of Pt_{15} inside and outside the CNT, as shown in Fig. 4a. In the plots, the Fermi level (E_f) is defined as the energy zero. We found that these CNT supported systems exhibit a metallic character with a high density of states at the Fermi level. It is interesting to note that the Pt 5d states are in fact quite similar for the Pt clusters inside and outside the CNT. In particular, the calculated Pt d-band center[52] difference between the Pt_{15} inside and outside the CNT is within 0.2 eV (−2.10 eV for the inside and −2.27 eV for the outside). The Bader charge[53] of Pt_{15}@CNT and Pt_{15}–CNT were also calculated, and are listed in Table 1, which shows that the Pt cluster donates electrons to the CNT in both cases, and the overall (net) charge of the Pt cluster are similar, being ∼+0.6 $|e|$. Obviously, the electronic structure alone cannot predict the catalytic activity of the Pt particles.

The catalyst activity of Pt_{15} inside and outside the CNT was then examined by DFT calculations, using O_2 dissociation ($O_2 \rightarrow 2O$) as the probe reaction. O_2 dissociation is an elementary reaction step occurring in many catalytic oxidation reactions, as well as in the electrocatalytic oxygen reduction reaction (ORR), where Pt is found to be one of the best catalysts for O_2 activation.[42]

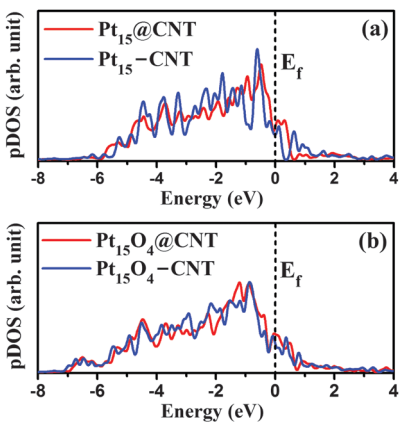

Fig. 4 Projected density of states (pDOSs) onto the 5d of Pt atoms in Pt_{15} and $Pt_{15}O_4$ inside and outside the CNT. The Fermi level (E_f) is set as energy zero.

Table 1 Bader charges (Q, unit $|e|$) of CNT supported Pt_{15} and $Pt_{15}O_4$

		Outside CNT	Inside CNT
Pt_{15}	Q_{Pt}[a]	0.59	0.61
$Pt_{15}O_4$	Q_{Pt}	3.16	2.71
	Q_O	−2.97	−2.91

[a] Q_{Pt} and Q_O are the total (net) charge on all Pt and O atoms, respectively.

For ORR, a key challenge is to increase the activity (reduce the overpotential) and stability (anticorrosion) of the carbon-supported Pt electrode at high potentials.[43,54] It should be borne in mind that the ORR on Pt under electrochemical conditions should involve not only an O_2 direct dissociation channel, but also a coupled proton electron transfer channel ($O_2 + H^+ + e^- \rightarrow HO_2^* \rightarrow \cdots OH^*$ and H_2O), as discussed in our previous work.[42] The purpose of this study is to demonstrate the activity difference for Pt nanoparticle inside and outside CNTs using O_2 dissociation as a model reaction.

To compare the O_2 dissociation activity and the material stability, we gradually added O_2 molecules into the two systems, and the trend of O_2 activation with the increase in O atom coverage was thus determined. Specifically, we investigated the O_2 molecular adsorption and dissociation on Pt_{15}, $Pt_{15}O_2$, $Pt_{15}O_4$, and $Pt_{15}O_6$ particles inside and outside the CNT, where each adsorbed molecular O_2 can dissociate into two O atoms (the calculated barrier was found to be feasible at these stages, see below). For example, at the $Pt_{15}O_6$ stage, there are three O_2 molecules that adsorb and dissociate sequentially on Pt_{15}, as depicted in Fig. 5. Considering that the O atoms may well reconstruct the Pt particle, the SSW method integrated with the DFT calculations was again utilized to explore the PES of the structures at a middle O coverage, *i.e.* $Pt_{15}O_4$–CNT and $Pt_{15}O_4$@CNT, and thus the effects on the activity due to the restructuring could be taken into account. While the SSW structure search is generally performed with CNT fixed, we also tested the SSW search with CNT fully relaxed, and found that the CNT is not oxidized, because the oxidation of the CNT wall tends to increase the energy of the system considerably (from the SSW trajectories), which is attributed to the fact that Pt–O bonding is preferred over C–O bonding.

Herein, we provide a detailed account on the identified $Pt_{15}O_4$ GS structures inside and outside the CNT. By inspecting the Pt_{15} skeleton, we found that both GS structures (Fig. 5b) largely deviate from the original Pt_{15} structure in the absence of O atoms (Fig. 1, top panel). In particular, for the $Pt_{15}O_4$@CNT, most of the O atoms (three of them) are distributed at the two ends of the cluster, while one O atom is located at the middle of the Pt_{15} rod. The two-ends of the O atoms are two-coordinated and the middle O atom is three coordinated with the Pt atoms. The Pt_{15} rod is further elongated and distorted, due to the adsorption of the O atoms. The results from the SSW structure search indicates that the dissociated O atoms are possibly diffused into the middle layers of the particle (to maximize the bonding), and not limited to bonding with the Pt atoms

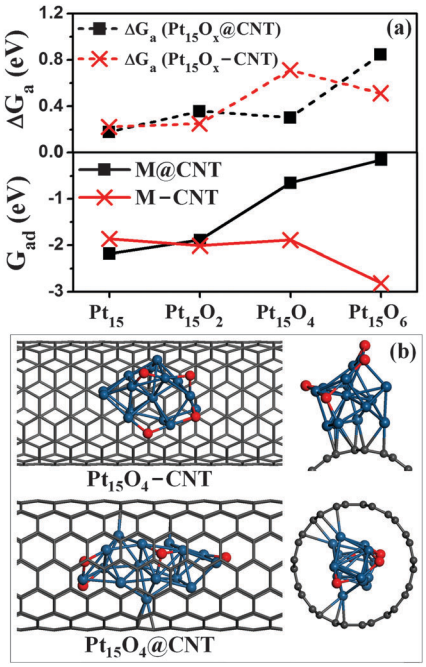

Fig. 5 (a) The O_2 adsorption energies (G_{ad}) and the free energy barriers (ΔG_a) of O–O bond breaking on supported Pt_{15} systems at different O coverage. (b) The GS structures for $Pt_{15}O_4$–CNT and $Pt_{15}O_4$@CNT from the SSW search.

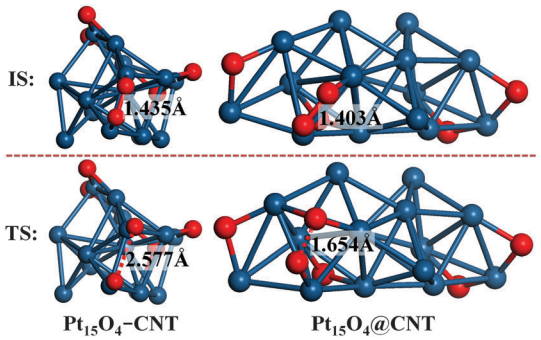

Fig. 6 Optimized initial and transition state (ISs and TSs) structures of O–O direct dissociation on $Pt_{15}O_4$–CNT (left) and $Pt_{15}O_4$@CNT (right). To better illustrate the local bonding, not all the carbon atoms of CNT are shown.

exposed at the two terminals, which should be of great importance for catalysis at finite temperatures. In fact, the structure mobility of the Pt clusters inside CNT is still large, as shown in Fig. 2, and thus they cannot be simply treated as rigid rods.

On the other hand, for $Pt_{15}O_4$–CNT, the bonding pattern of Pt–O is similar, being an O–Pt–O staple-like structure with the middle Pt atom being pulled out from the cluster. Each O atom is two-coordinated and all the O atoms are located away from the Pt–C interface (see Fig. 5b). As a result, the original Pt_{15} symmetry (C_{2v}) is destroyed and the number of interfacial Pt atoms (Pt interacting with CNT) is reduced from six to five, in order to maximize the Pt–O bonding (the Pt–O bonding is stronger than the Pt–CNT interaction).

As for charging Pt in the presence of O atoms, we found that the Pt cluster becomes much more positively charged in the presence of O atoms (Table 1), showing the large electronegativity of the O atoms. At the stage of $Pt_{15}O_4$, the difference between the Pt inside and Pt outside starts to emerge; the Pt cluster outside the CNT can donate more electrons and is thus, more positively charged.

Catalytic activity in O_2 dissociation. The adsorption free energy of the O_2 molecule (G_{ad}) and the dissociation barrier (ΔG_a) for $O_2 \rightarrow 2O$ were computed using DFT by locating the most stable O_2 adsorption state at each stage and the O–O bond breaking TSs. G_{ad} was defined as the free energy change for each O_2 molecule upon adsorption from the gas phase (at standard conditions) to the Pt particle (*i.e.* the differential adsorption energy, also see calculation details). It should be emphasized that because there are a number of possible adsorption sites and O–O dissociation sites, we generally consider a series of likely sites around the particles, so only the highest adsorption energy (the most stable) and the lowest dissociation barrier are reported in Fig. 5 (these structures are listed in the ESI† for reference) and utilized for comparison of the activity. The details for calculating the free energy of O_2 dissociation can be found in the calculation details and also in our previous work.[42] The most stable O_2 adsorption geometries on CNT supported Pt_{15} and $Pt_{15}O_4$ are illustrated in the ESI,† Fig. S5, which show that O_2 molecules tend to bond with the low coordinated Pt atoms at the terminal sites of the clusters. In Fig. 6, we highlight the located structures for the initial states (ISs) and TSs for O_2 dissociation on $Pt_{15}O_4$. With the increase of the O coverage, the adsorption of O_2 molecules tends to avoid the preadsorbed O atoms, indicating a strong repulsion between the adsorbed O atom and the O_2 molecule. On the other hand, no clear correlation between the O adsorption sites and their C-bonding proximity are observed in both cases.

In general, we found that the trend of G_{ad} with the increase of O coverage for Pt_{15}@CNT was opposite to that of Pt_{15}–CNT. We noticed that the G_{ad} had no clear relation with the charge of the Pt cluster (see Table 1). For example, G_{ad} remains quite constant from Pt_{15}–CNT to Pt_{15} O_4–CNT, but the charge state of all the Pt atoms increase dramatically (from +0.59 to +3.16). On the other hand, G_{ad} is much lower at the $Pt_{15}O_4$@CNT stage compared to at Pt_{15}@CNT. We expect that the other effects, in addition to the Pt charge state, such as the interaction between CNT and O_2, the local repulsive interaction between preadsorbed O atoms and the adsorbed O_2, should also be considered for O_2 adsorption.

Importantly, at high O coverage, the activity for Pt inside and outside the CNT becomes rather different. On bare Pt_{15}@CNT, molecular O_2 can adsorb strongly, with a large adsorption energy ($G_{ad} \sim -2$ eV), and it can dissociate readily ($\Delta G_a < 0.2$ eV). With the increase in O coverage, the O atoms gradually terminate the two ends of the Pt rod and the sites available for further O_2 adsorption and dissociation become limited. On $Pt_{15}O_4$@CNT, they are still active for dissociating O_2, with ΔG_a being 0.30 eV, much lower than the typical value ($\sim$0.65 eV) for O_2 dissociation on large Pt particles and for Pt(111) in the steady state.[42,43] At the TS of O_2 dissociation on $Pt_{15}O_4$@CNT, one O atom sits at the bridge site and the other O atom sits at the top site. The O–O bond length of the

adsorbed O_2 at the TS is 1.65 Å, similar to that of ORR on the Pt(111) surface[36] (~1.8 Å).

When further increasing the O coverage, we found that on $Pt_{15}O_6$@CNT, the G_{ad} of O_2 is only −0.15 eV and ΔG_a reaches to 0.85 eV, which indicates that O_2 activation becomes kinetically difficult at this high O coverage at ambient temperature, since the adsorbed O_2 molecule prefers to desorb. It is thus expected that O_2 dissociation/removal will achieve an equilibrium on $Pt_{15}O_4$ if the newly-arrived two O atoms in $Pt_{15}O_6$@CNT react as oxidants, *e.g.*, to form H_2O in the ORR. Overall, the CNT confined Pt particles can be stable under ambient aerobic conditions.

In contrast, Pt_{15}–CNT exhibits an irreversible behavior for O_2 activation until the particle is finally oxidized. With the increase of O coverage, the Pt particle expands in volume and is distorted largely away from its GS structure at zero O coverage. At the $Pt_{15}O_4$–CNT stage, the O_2 dissociation activity is in fact poorer than that of $Pt_{15}O_4$@CNT, since the calculated barrier is more than 0.7 eV, ~0.4 eV higher than that of $Pt_{15}O_4$@CNT. At the TS of O_2 dissociation on $Pt_{15}O_4$–CNT, the two O atoms sit atop two sites of Pt, with a dissociating O–O distance of 2.58 Å, which is significantly longer than that for the ORR on the Pt(111) surface[42] (~1.8 Å) and that for O_2 dissociation on $Pt_{15}O_4$@CNT (1.65 Å, Fig. 6).

To understand the activity difference between $Pt_{15}O_4$@CNT and $Pt_{15}O_4$–CNT, we calculated the metal d-band, as shown in Fig. 4b, in which we did not, however, identify any obvious difference between $Pt_{15}O_4$@CNT and $Pt_{15}O_4$–CNT. The difference between the calculated Pt d-band center of the two systems is small, *i.e.* 0.13 eV (−2.25 eV for the inside and −2.38 eV for the outside), and thus cannot rationalize the large difference calculated in the activity for O_2 dissociation. Next, by calculating the Bader charge for the IS, TS, and FS of O_2 dissociation, as listed in Table 2, we can obtain the direction of electron transfer during the reaction. In general, electrons flow from both the Pt atoms and the CNT to the newly arrived O_2 molecule and the dissociated O atoms. The charge of the Pt cluster outside and inside the CNT increases by +0.29 $|e|$ and +0.54 $|e|$ in the reaction, respectively, which is attributed mainly to the Pt atoms at the reaction center, apparently because the adsorbed O atoms require more electrons than the adsorbed O_2 molecule. In the reaction, the CNT also helps to provide electrons to the reaction center, but to a minor extent. The major difference between the charge of Pt_{15} inside the CNT and outside the CNT occurs at the TS, which indicates that the position of the TS plays an important role in reducing the barrier of O_2 dissociation on $Pt_{15}O_4$@CNT.

Indeed, by comparing the geometry of the located TSs (Fig. 6), we attribute the lower activity of the $Pt_{15}O_4$–CNT to the lack of a favorable local site for O–O dissociation, as only two Pt atoms are involved at the TS but there are three Pt atoms at the TS on $Pt_{15}O_4$@CNT. This is apparently because the Pt cluster outside the CNT is more rigid and highly distorted by the adsorbed O atoms, as depicted in the GS structure of $Pt_{15}O_4$–CNT. When the O–O bond breaks, the neighboring Pt atoms cannot easily adjust their geometries to facilitate the dissociation reaction.

Table 2 The relative Bader charge (ΔQ, unit $|e|$) during O_2 dissociation on CNT supported $Pt_{15}O_4$. All ΔQ (at the IS, TS, and FS) were calculated with respect to the Bader charge Q before the adsorption of the O_2 molecule (data shown in Table 1). Listed data include ΔQ on all the Pt atoms, the Pt atoms at the reaction center (abbreviated as Pt-re, Pt atoms interacting directly with the dissociating O2), and CNT

		Outside CNT	Inside CNT	Difference
IS	ΔQ_{Pt}	0.60	0.44	0.16
	$\Delta Q_{Pt\text{-}re}$	0.63	0.49	0.14
	ΔQ_{CNT}	0.20	0.22	−0.02
TS	ΔQ_{Pt}	0.78	0.74	0.04
	$\Delta Q_{Pt\text{-}re}$	0.92	0.67	0.25
	ΔQ_{CNT}	0.39	0.16	0.23
FS	ΔQ_{Pt}	0.89	0.98	−0.09
	$\Delta Q_{Pt\text{-}re}$	0.92	0.92	0.00
	ΔQ_{CNT}	0.36	0.35	0.01

Finally, at the $Pt_{15}O_6$–CNT stage, the particle starts to get oxidized, with the Pt–Pt bonds becoming significantly lengthened by the adsorbed O atoms and the G_{ad} of O_2 decreasing rapidly to ~−3 eV, due to the formation of low oxidation state Pt cations. O_2 dissociation can still occur on $Pt_{15}O_6$–CNT, with the calculated barrier being less than 0.7 eV, indicating that the Pt cluster will be eventually oxidized. This result is consistent with the common observation in catalysis that small Pt particles are highly vulnerable to oxidation under aerobic reaction conditions.[55]

Discussion. It was suspected that the CNT inside/outside nanoparticles might have different catalytic performances, and recent experiments by Bao's group[19] and Guo's group[23] indeed showed evidence for Ru, Pd, and Pt metal, and RhMn alloy inside/outside CNTs for N_2 dissociative adsorption, benzene hydrogenation reactions, methanol oxidation and CO dissociation. In particular, Bao's group[16,17] showed that Fe nanoparticles inside and outside MWCNTs have distinct anticorrosion ability in an O_2 atmosphere. The oxidation of metallic Fe nanoparticles inside CNTs (4–8 nm in diameter) to Fe_2O_3 occur at a temperature of ~70–115 °C, higher than that of the outside metal catalyst. For Pt nanoparticles, Guo and his coworkers[23] also found that Pt nanoparticles inside large CNTs (~80 nm in diameter) can display much better durability than Pt nanoparticles outside the CNTs in methanol electro-oxidation. After 600 cyclic voltammetry cycles, only a small loss (<10%) was detected in the current density for Pt inside CNTs, while a 44.6% loss and 73.5% loss were detected for Pt outside CNTs and commercial Pt/C catalyst, respectively. However, the fundamental origin for the CNT enhanced catalytic performance of the composite catalyst remains unclear, although it is generally accepted that the metal component should be the active site.

These previous studies have discussed the influence of the carbon support on the catalyst activity, mainly based on the static structure of the metal nanoparticle, such as the charge transport between the substrate and metal,[56,57] the quantum size effect,[55] the molecular adsorption and diffusion (mass transport)[18,58] and the substrate structure.[21,59] For example, mass transport is a general concern for Metal@CNT, since it is expected that the molecular diffusion is limited inside the CNT. However, it was

experimentally found that the catalytic activity of the Metal@CNT is often much higher than that of Metal/CNT (see ref. 18, 19, 23 and 24). This indicates that mass transport might not be a key reason for the activity difference and a better understanding of the chemical reactions, *e.g.*, the rate-limiting step, is essential.

This work shows that the configuration space of nanoparticles could be a key factor for making active and stable catalysts. Because chemical reactions on metal surfaces are often highly exothermic, *e.g.* 1.5 eV per O atom for O_2 dissociation on Pt_{15}, bare metal nanoparticles have a strong tendency to reconstruct under reaction conditions. In contrast to outside CNTs, the structure versatility of metal nanoparticles inside CNTs increases at the low energy region, due to the extra metal-substrate bonding, but then decreases at high energy regions, owing to the spatial confinement. The former facilitates the creation of favorable catalytic sites for reaction, and the latter can prevent the structure of the particle being destroyed (*e.g.*, being oxidized) by the catalytic reaction. Therefore, the confined Pt particle possesses both high activity for O_2 activation and high stability against high O coverage. This may explain in general the enhanced stability of metal particles (*e.g.*, Fe and Pt) inside the CNT.[16,17,23] Our results indicate that not only the strength, but also the shape of the substrate-metal interaction potential need to be optimized for the design of better catalysts.

4. Conclusions

This work covers a theoretical survey on the structure and oxidation tendency of porous material supported metal nanoparticles. Using the SSW global optimization method, we investigated the PES of Pt particles inside and outside the CNTs, based on which the effects of the CNT to the catalyst structure, activity, and stability were analyzed. The theory demonstrates that the interaction between the metal particle and the supporting material can significantly alter the PES of the metal particle and lead to unexpected structure dynamic features. Our main conclusions are outlined as follows.

The configuration space of Pt nanoparticles inside and outside CNTs shows distinct features. Compared to the nanoparticles outside the CNT, Pt nanoparticles inside the CNT are structurally more flexible at low temperatures (note that the GS structure itself does not deform any more significantly), but have much less liquid-like structure configurations at high temperature. The landscape of the PES of the Pt nanoparticles inside the CNT exhibit two obvious funnels, corresponding to the fcc packing structures and the twisted rod structures. These structural differences are reflected by the fact that the peak of the heat capacity C_v curve for the nanoparticle inside the CNT shifts towards the low temperature region.

Using O_2 dissociation as the probe reaction, we found that the O_2 dissociation could occur readily on both the Pt_{15} particles inside and outside CNTs at low O coverages. However, at higher O coverage, the particles inside the CNTs become catalytically more active for O_2 dissociation and also resistant to high oxidation by the dissociated O atoms. The higher activity for the particles inside the CNTs is attributed to the exposure of the favorable reaction sites for O_2 dissociation. The major problem for the particles outside the CNTs is high oxidation with the increase in O coverage, as reflected by the strong exothermicity in the adsorption of O_2 molecules.

Acknowledgements

We acknowledge the National Science foundation of China (21173051, 21361130019), 973 program (2011CB808500, 2013CB834603), the Science and Technology Commission of Shanghai Municipality (08DZ2270500), the Program for Professor of Special Appointment (Eastern Scholar) at Shanghai Institute of Higher Learning, China Postdoctoral Science Foundation funded project (2013M531112), and the Shanghai Postdoctoral Scientific Program (13R21410300) for financial support.

References

1 G. Ertl, *Angew. Chem., Int. Ed.*, 2008, **47**, 3524–3535.
2 N. M. Markovic and P. N. Ross, *Surf. Sci. Rep.*, 2002, **45**, 121–229.
3 G. A. Somorjai, *Surf. Sci.*, 1994, **299**, 849–866.
4 F. Tao and M. Salmeron, *Science*, 2011, **331**, 171–174.
5 A. F. Lee, C. V. Ellis, J. N. Naughton, M. A. Newton, C. M. A. Parlett and K. Wilson, *J. Am. Chem. Soc.*, 2011, **133**, 5724–5727.
6 F. Tao, M. E. Grass, Y. W. Zhang, D. R. Butcher, J. R. Renzas, Z. Liu, J. Y. Chung, B. S. Mun, M. Salmeron and G. A. Somorjai, *Science*, 2008, **322**, 932–934.
7 S. Helveg, C. Lopez-Cartes, J. Sehested, P. L. Hansen, B. S. Clausen, J. R. Rostrup-Nielsen, F. Abild-Pedersen and J. K. Norskov, *Nature*, 2004, **427**, 426–429.
8 P. L. Hansen, J. B. Wagner, S. Helveg, J. R. Rostrup-Nielsen, B. S. Clausen and H. Topsoe, *Science*, 2002, **295**, 2053–2055.
9 C. Mager-Maury, G. Bonnard, C. Chizallet, P. Sautet and P. Raybaud, *ChemCatChem*, 2011, **3**, 200–207.
10 P. Raybaud, C. Chizallet, C. Mager-Maury, M. Digne, H. Toulhoat and P. Sautet, *J. Catal.*, 2013, **308**, 328–340.
11 C. Shang and Z. P. Liu, *J. Chem. Theory Comput.*, 2013, **9**, 1838–1845.
12 X. J. Zhang, C. Shang and Z. P. Liu, *J. Chem. Theory Comput.*, 2013, **9**, 3252–3260.
13 V. Georgakilas, D. Gournis, V. Tzitzios, L. Pasquato, D. M. Guldi and M. Prato, *J. Mater. Chem.*, 2007, **17**, 2679–2694.
14 S. J. Liao, K. A. Holmes, H. Tsaprailis and V. I. Birss, *J. Am. Chem. Soc.*, 2006, **128**, 3504–3505.
15 Y. Y. Liang, H. L. Wang, P. Diao, W. Chang, G. S. Hong, Y. G. Li, M. Gong, L. M. Xie, J. G. Zhou, J. Wang, T. Z. Regier, F. Wei and H. J. Dai, *J. Am. Chem. Soc.*, 2012, **134**, 15849–15857.
16 W. Chen, X. L. Pan, M. G. Willinger, D. S. Su and X. H. Bao, *J. Am. Chem. Soc.*, 2006, **128**, 3136–3137.
17 W. Chen, X. L. Pan and X. H. Bao, *J. Am. Chem. Soc.*, 2007, **129**, 7421–7426.
18 D. H. Deng, L. Yu, X. Q. Chen, G. X. Wang, L. Jin, X. L. Pan, J. Deng, G. Q. Sun and X. H. Bao, *Angew. Chem., Int. Ed.*, 2013, **52**, 371–375.

19 X. L. Pan and X. H. Bao, *Acc. Chem. Res.*, 2011, **44**, 553–562.
20 D. H. Chi, N. T. Cuong, N. A. Tuan, Y. T. Kim, H. T. Bao, T. Mitani, T. Ozaki and H. Nagao, *Chem. Phys. Lett.*, 2006, **432**, 213–217.
21 D. Duca, F. Ferrante and G. La Manna, *J. Phys. Chem. C*, 2007, **111**, 5402–5408.
22 M. Gong, Y. G. Li, H. L. Wang, Y. Y. Liang, J. Z. Wu, J. G. Zhou, J. Wang, T. Regier, F. Wei and H. J. Dai, *J. Am. Chem. Soc.*, 2013, **135**, 8452–8455.
23 J. N. Zhang, S. J. Guo, J. Y. Wei, Q. Xu, W. F. Yan, J. W. Fu, S. P. Wang, M. J. Cao and Z. M. Chen, *Chem. – Eur. J.*, 2013, **19**, 16087–16092.
24 Z. J. Chen, Z. H. Guan, M. R. Li, Q. H. Yang and C. Li, *Angew. Chem., Int. Ed.*, 2011, **50**, 4913–4917.
25 D. J. Cheng, W. C. Wang and S. P. Huang, *J. Phys. Chem. C*, 2007, **111**, 1631–1637.
26 L. L. Wang and D. D. Johnson, *J. Am. Chem. Soc.*, 2007, **129**, 3658–3664.
27 H. J. Zhai, Y. F. Zhao, W. L. Li, Q. Chen, H. Bai, H. S. Hu, Z. A. Piazza, W. J. Tian, H. G. Lu, Y. B. Wu, Y. W. Mu, G. F. Wei, Z. P. Liu, J. Li, S. D. Li and L. S. Wang, *Nat. Chem.*, 2014, **6**, 727–731.
28 J. M. Soler, E. Artacho, J. D. Gale, A. Garcia, J. Junquera, P. Ordejon and D. Sanchez-Portal, *J. Phys.: Condens. Matter*, 2002, **14**, 2745–2779.
29 J. Junquera, O. Paz, D. Sanchez-Portal and E. Artacho, *Phys. Rev. B: Condens. Matter Mater. Phys.*, 2001, **64**, 235111.
30 N. Troullier and J. L. Martins, *Phys. Rev. B: Condens. Matter Mater. Phys.*, 1991, **43**, 1993–2006.
31 J. P. Perdew, K. Burke and M. Ernzerhof, *Phys. Rev. Lett.*, 1996, **77**, 3865–3868.
32 J. H. Wu and F. Hagelberg, *Phys. Rev. B: Condens. Matter Mater. Phys.*, 2009, **79**, 115436.
33 J. H. Wu and F. Hagelberg, *ChemPhysChem*, 2013, **14**, 1696–1702.
34 A. P. Sutton and J. Chen, *Philos. Mag. Lett.*, 1990, **61**, 139–146.
35 S. P. Huang and P. B. Balbuena, *Mol. Phys.*, 2002, **100**, 2165–2174.
36 B. H. Morrow and A. Striolo, *J. Phys. Chem. C*, 2007, **111**, 17905–17913.
37 H. F. Wang and Z. P. Liu, *J. Am. Chem. Soc.*, 2008, **130**, 10996–11004.
38 C. Shang and Z. P. Liu, *J. Chem. Theory Comput.*, 2010, **6**, 1136–1144.
39 J. K. Norskov, J. Rossmeisl, A. Logadottir, L. Lindqvist, J. R. Kitchin, T. Bligaard and H. Jonsson, *J. Phys. Chem. B*, 2004, **108**, 17886–17892.
40 D. C. Ford, A. U. Nilekar, Y. Xu and M. Mavrikakis, *Surf. Sci.*, 2010, **604**, 1565–1575.
41 Y. H. Fang and Z. P. Liu, *J. Am. Chem. Soc.*, 2010, **132**, 18214.
42 G. F. Wei, Y. H. Fang and Z. P. Liu, *J. Phys. Chem. C*, 2012, **116**, 12696–12705.
43 G. F. Wei and Z. P. Liu, *Phys. Chem. Chem. Phys.*, 2013, **15**, 18555–18561.
44 X. Wang and D. Tian, *Comput. Mater. Sci.*, 2009, **46**, 239–244.
45 J. P. K. Doye and D. J. Wales, *New J. Chem.*, 1998, **22**, 733–744.
46 C. H. Hu, C. Chizallet, C. Mager-Maury, M. Corral-Valero, P. Sautet, H. Toulhoat and P. Raybaud, *J. Catal.*, 2010, **274**, 99–110.
47 C. J. Tsai and K. D. Jordan, *J. Phys. Chem.*, 1993, **97**, 11227–11237.
48 J. P. K. Doye and D. J. Wales, *Phys. Rev. Lett.*, 1998, **80**, 1357–1360.
49 J. A. Thomas and A. J. H. McGaughey, *J. Chem. Phys.*, 2008, **128**, 084715.
50 K. Koga, G. T. Gao, H. Tanaka and X. C. Zeng, *Nature*, 2001, **412**, 802–805.
51 Z. P. Liu and P. Hu, *J. Am. Chem. Soc.*, 2003, **125**, 1958–1967.
52 B. Hammer and J. K. Norskov, *Surf. Sci.*, 1995, **343**, 211–220.
53 R. F. W. Bader, *Chem. Rev.*, 1991, **91**, 893–928.
54 G. F. Wei and Z. P. Liu, *Energy Environ. Sci.*, 2011, **4**, 1268–1272.
55 T. Imaoka, H. Kitazawa, W.-J. Chun, S. Omura, K. Albrecht and K. Yamamoto, *J. Am. Chem. Soc.*, 2013, **135**, 13089–13095.
56 L. Yu, W. X. Li, X. L. Pan and X. H. Bao, *J. Phys. Chem. C*, 2012, **116**, 16461–16466.
57 H. L. Gao and J. J. Zhao, *J. Chem. Phys.*, 2010, **132**, 234704.
58 D. H. Lim and J. Wilcox, *J. Phys. Chem. C*, 2012, **116**, 3653–3660.
59 N. T. Cuong, A. Fujiwara, T. Mitani and D. H. Chi, *Comput. Mater. Sci.*, 2008, **44**, 163–166.